

Analysis of a deformable fracture in permeable material

Lawrence C. Murdoch^{1,*},† and Leonid N. Germanovich^{2,‡}

¹ *Department of Geosciences, Clemson University, 340 Brackett Hall, Clemson, SC 29634, U.S.A.*

² *Georgia Institute of Technology, School of Civil Engineering, 790 Atlantic Drive,
Mason Building, Atlanta, GA 30332-0355, U.S.A.*

SUMMARY

The response of deformable fractures to changes in fluid pressure controls phenomena ranging from the flow of fluids near wells to the propagation of hydraulic fractures. We developed an analysis designed to simulate fluid flows in the vicinity of asperity-supported fractures at rest, or fully open fractures that might be propagating. Transitions between at-rest and propagating fractures can also be simulated. This is accomplished by defining *contact aperture* as the aperture when asperities on a closing fracture first make contact. Locations on a fracture where the aperture is less than the contact aperture are loaded by both fluid pressure and effective stress, whereas locations where the aperture exceeds the contact aperture are loaded only by fluid pressure. Fluid pressure and effective stress on the fracture are determined as functions of time by solving equations of continuity in the fracture and matrix, and by matching the global displacements of the fracture walls to the local deformation of asperities.

The resulting analysis is implemented in a numerical code that can simulate well tests or hydraulic fracturing operations. Aperture changes during hydraulic well tests can be measured in the field, and the results predicted using this analysis are similar to field observations. The hydraulic fracturing process can be simulated from the inflation of a pre-existing crack, to the propagation of a fracture, and the closure of the fracture to rest on asperities or proppant. Two-dimensional, multi-phase fluid flow in the matrix is included to provide details that are obscured by simplifications of the leakoff process (Carter-type assumptions) used in many hydraulic fracture models. Execution times are relatively short, so it is practical to implement this code with parameter estimation algorithms to facilitate interpretation of field data. Copyright © 2006 John Wiley & Sons, Ltd.

KEY WORDS: hydraulic fracturing; deformable fracture; fracture asperities; Darcy flow; leakoff; fracture closure

*Correspondence to: Lawrence C. Murdoch, Department of Geosciences, Clemson University, 340 Brackett Hall, Clemson, SC 29634, U.S.A.

†E-mail: lmurdoch@clemson.edu

‡E-mail: leonid@ce.gatech.edu

Contract/grant sponsor: National Science Foundation; contract/grant numbers: EAR 9876124, EAR 0001146, OCE-0221974, OCE-0242163, CMC 0421090

INTRODUCTION

Fractures in earth materials deform by dilating or contracting when the fluid pressure within them changes [1]. This process is largely responsible for the recovery of petroleum or water from wells drilled into reservoirs or aquifers of fractured rock. In those cases, decreases in fluid pressure in a well cause fracture apertures to diminish, thereby reducing fluid storage. In other applications, fluid is injected into wells to dilate existing fractures or to create new ones in an effort to improve the performance of the wells. The process of hydraulic fracturing is widely used to stimulate the production of wells in petroleum reservoirs and aquifers [2,3], or to improve environmental remediation [4,5]. *In situ* stresses can also be estimated using hydraulic fracturing [6–8], where the history of fluid pressure in a well is scrutinized to estimate when the opposing walls of a closing hydraulic fracture first make contact.

Existing simulation methods

Transient fluid flow in the vicinity of deformable fractures intersecting wells has been simulated using a wide range of approaches that depend on the particular application [1]. A key aspect of all the methods is interaction between the fluid flow and deformation of fractures and the enveloping matrix. The simplest approach is to assume that changes in storage result from deformations in response to local pressure changes, and that the flow properties are independent of fluid pressure. In this case, the flow in the vicinity of a fracture intersecting a well could resemble flow in a confined aquifer composed of porous media. This assumption allows fractured media to be analysed as equivalent porous media [9] and many analytical and numerical methods are available for wells in single or dual-porosity media [10–17].

More advanced analyses consider discrete fractures of various geometries. Rutqvist [18] considered flow in the vicinity of a single, idealized deformable fracture in order to explain the results of a variety of field experiments, and his work stands as one of the most comprehensive combinations of theoretical and field analyses of deformable fractures. Other models consider arrays of discrete fractures of various locations, densities and sizes [19–22]. Some models simulate fractures as large arrays of rigid or slightly compressible conduits and ignore explicit evaluation of stresses because they are primarily interested in simulating transport during steady flows [23,24]. In other cases, the use of a slightly compressible formulation that ignores explicit changes in aperture appears to be sufficient to analyse some problems involving well tests or flow through aquifers [25,26]. Some transport processes, such as storage of nuclear waste or recovery from formations with pressure-sensitive permeability, do involve conditions where aperture change could be significant (e.g. References [27,28]) and codes have been developed to evaluate these effects [27–33]. Elastic deformation of irregular asperities on fracture surfaces is considered explicitly in some methods [34], and this approach has recently been extended to consider arrays of discrete fractures with rough surfaces [35,36]. All of these discrete-fracture models appear to be limited to static arrays; that is, they do not consider propagation. An array of vertical fractures propagating in a horizontal direction within a stratigraphic layer was analysed by Germanovich *et al.* [37].

A wide range of models have been put forth to simulate fractures propagating near well bores [38]. Considerable advances have been made in numerical methods for determining the forms of fractures in 3-D [39] and in analytical methods for determining the pressures and apertures in propagating fractures [37,40–45]. These analyses consider coupling between flow along the

fracture and changes in aperture resulting from mechanical deformation of the matrix. All the fracture propagation models include explicit calculation of stresses and displacements, but they commonly simplify the evaluation of fluid flow in the vicinity of the fracture. Some analytical solutions of propagating hydraulic fractures ignore fluid flow out of the fracture, the so-called *leakoff*, altogether. Analytical and numerical solutions that do include leakoff [37,45] will commonly use simple analytical expressions (e.g. Reference [46]) to characterize this process.

Both the discrete-fracture models derived for hydrology and the propagation models developed for petroleum applications can analyse coupling between fluid flow and deformation, although some processes represented by both groups of models have been represented in simplified ways. The discrete-fracture models are suited to simulating flow and transport through networks of fractures with complex geometry. None of the discrete-fracture models can simulate fracture propagation, however, and only some of them can explicitly calculate stresses and displacements. The propagation models can calculate stresses and displacements, but they only crudely approximate fluid flow in the matrix enveloping the fracture, and they are unable to simulate the displacement response caused by injection into natural fractures.

The purpose of this paper is to describe a model that includes some of the attributes of both discrete-fracture and propagation analyses. This hybrid model will consider a well intersecting a single fracture that rests on asperities under ambient conditions, but it can dilate and propagate as a result of injection. As a result, the analysis can consider natural fractures and fractures induced by fluid injection. Stresses and displacements are analysed using methods similar to propagation models, but the matrix is considered to be variably saturated and fairly general fluid flow processes are allowed. Combining attributes from these two classes of models will provide results that are currently unavailable.

Conceptual model of a natural deformable fracture

Most fractures at depth in earth materials are partially open, with at least some of the fracture surface pinched closed by contact with asperities on the opposing surfaces, or bridges of intact material spanning fracture segments [1,47–50]. It will be convenient to assume as an initial state that a fracture is supported in part by fluid pressure in its open sections and in part by stresses on contacting asperities [35,51]. For simplicity, it will also be assumed that the fracture lies normal to the direction of least principle compression, so shear stresses in the plane of the fracture can be ignored.

The matrix is assumed to be mechanically homogeneous and uniformly stressed prior to development of the fracture. The length of the fracture is finite and mechanical interactions with neighbouring cracks as well as fluid flow through cross-cutting fractures can be taken into account by adjusting the permeability of the matrix. This is possible when the neighbouring fractures are considerably smaller than the one under consideration.

Pressures will change during fluid flow in the fracture, and this will change stresses on the contacting asperities. Decreasing the fluid pressure will compress asperities and cause the aperture to diminish, whereas increasing the fluid pressure will extend asperities and increase the aperture (Figure 1; [35,47]).

Continuing to decrease fluid pressure will only continue to compress asperities, but continuing to increase fluid pressure will diminish the asperity stress and cause opposing asperities to separate (Figure 1). Presumably, further increase in fluid pressure will continue to separate asperities, and to increase the stress intensity at the tip of the fracture (stippled region

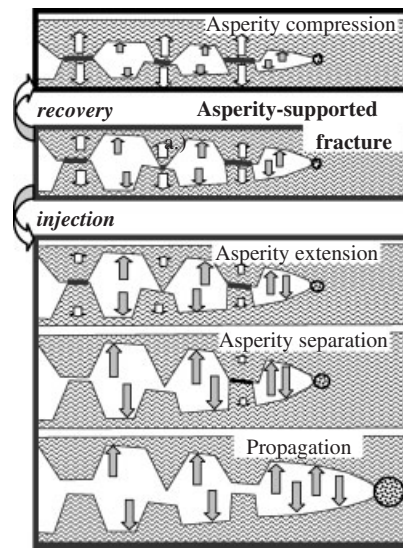


Figure 1. A half-fracture supported by stress on asperities (white arrows) and fluid pressure (grey arrows). Decreasing fluid pressure during recovery causes asperity compression, increasing pressure during injection causes asperity extension, separation, and fracture propagation.

at the tips of the fractures in Figure 1). At some point, the stress intensity could be great enough to cause propagation [52].

The general conceptual model consists of four different conditions caused by changing fluid pressures (Figure 1). A decrease in fluid pressure causes *asperity compression* and a reduction in aperture (Figure 1). An increase in fluid pressure first causes *asperity extension* and then *asperity separation* (Figure 1; [35,51]). *Propagation* follows asperity separation when fluid pressures increase sufficiently (Figure 1). A reduction in fluid pressure following propagation would cause the opposite sequence of events as the fracture closes to rest on asperities.

For clarity with nomenclature (Appendix I), all the fractures described in the following pages will be much more transmissive than their enveloping matrix, so they can be considered open to fluid flow. However, we will reserve the use of the term *open fracture* to indicate fractures that are supported solely by fluid pressure, so the effective stresses on open fractures are zero. *Asperity-supported* fractures will refer to fractures where stresses on asperities or bridges at least partially support the fracture. Probably, most naturally occurring fractures at rest are asperity-supported.

DESCRIPTION OF THE MODEL

Processes inferred to occur during changes in fluid pressure will be represented in a theoretical model that considers deformation of the solid matrix and fluid flow within the fracture and matrix. Assumptions and principles used to develop the model will be described in the following pages. Equations, calculations and algorithms implemented in the model will be presented in

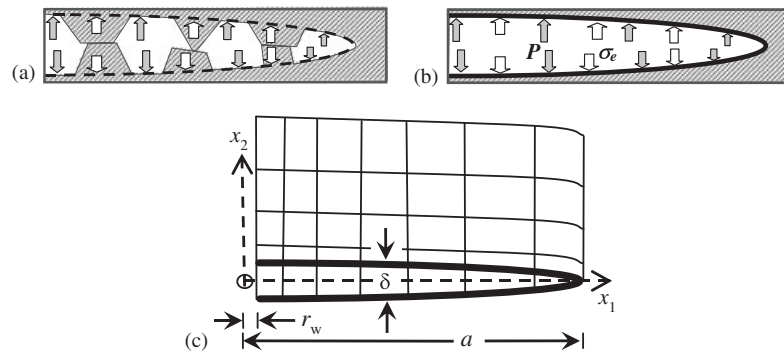


Figure 2. (a) Half-fracture resting on asperities; (b) represented as an elliptical cavity loaded by fluid pressure and effective stress; and (c) elliptical cavity divided into segments with finite-difference grid, coordinate axes, and dimensions used in the analysis.

Appendices A–H. We felt it was important to present details of the calculations used in the model, but this information has been included in appendices to avoid cluttering the description of assumptions and principles that follow.

The rough opposing surfaces of real fractures (Figure 2(a)) will be idealized by assuming the fracture is an elongated elliptical cavity in an elastic material, and the wall of the cavity is loaded arbitrarily by fluid pressure, P , and effective stress, σ_e (Figure 2(b)). Explicit consideration of the details of the deformation of asperities will be ignored and replaced by changes in effective stress and aperture. Therefore, the asperity stress represented in Figures 1 and 2(a) is averaged per unit area of the fracture and represented as σ_e (Figure 2(b)).

A uniform far-field compressive stress, σ_c , is assumed to confine the system. It follows that the *driving (net) pressure*, P_d , is the difference between the confining stress and the sum of the fluid pressure and effective stress for an asperity-supported fracture (Appendix B). *Aperture*, δ , is considered the average separation of two points that were adjacent in intact rock before the fracture formed.

Contact aperture, δ_o , is the aperture when asperities first lose contact during fracture opening, or make contact when it is closing. Contact aperture varies over a fracture face depending on the details of slight shear displacements, amplitude of asperities or roughness, thickness of mineral precipitates, or other factors that cause misalignment of opposing fracture walls. Proppant injected into a hydraulic fracture will increase contact aperture.

The distribution of contact aperture over the length of the fracture can be used to determine whether a fracture is open ($\delta > \delta_o$) and loaded only by fluid pressure, or asperity-supported and loaded by fluid pressure and effective stress ($\delta < \delta_o$). The distribution of contact aperture on fractures in the field is poorly known, but it is probably scale-dependant, increasing with the total length of the fracture (Appendix F).

The analysis will consider single, planar fractures of half-length, a , and aperture, δ , in two dimensions. The fracture will be normal to the x_2 coordinate and occur in the $x_2 = 0$ plane. Both rectangular plane-strain fractures, and circular axisymmetric fractures will be considered, and symmetry will allow both geometries to be represented in cross-section (Figure 2). The mouth of the fracture occurs in the wall of a borehole at $x_1 = r_w$, and the tip occurs at $x_1 = a$ (Figure 2). The fracture propagates in its initial plane, and it can open or close normal to this plane.

Fluid flow

Fluid flow occurs within the fracture and matrix, and fluid can exchange between these two regions. The fluid is assumed to be Newtonian and compressible. Matrix compressibility is considered during changes in fluid storage. Conservation of mass and momentum govern fluid flow within the fracture and matrix, and flow is assumed to be in the laminar regime. Several applications for this analysis are envisioned in the vadose zone, so partially saturated conditions in the matrix are assumed for generality. Note that incorporating non-Newtonian power-law, fluid in this analysis is straightforward.

Fluid flow in the fracture is considered in one dimension, so changes in fluid density normal to the flow direction within the fracture are ignored. Fluid flow in the matrix is considered as 2-D Darcy flow, and partially saturated conditions are allowed (Appendix A). This differs from the simplified Carter's [46] approximations of leakoff, q_L , used in most analyses of hydraulic fracturing.

Matrix deformation

Both global and local matrix deformations are assumed to occur. Global deformation of the fracture and enveloping matrix occurs in response to changes in the driving pressure (Appendix B) on the entire fracture face. In contrast, local deformation of asperities on the fracture surface occurs only in response to changes in local effective stress (Appendix E). These deformations are assumed to be equal [53].

All displacements are assumed to be linear elastic. However, the general relationship between effective stress and fracture aperture can be non-linear, because the area of contact between asperities increases with normal compressive stress in accordance with the results of laboratory experiments [54] and theoretical analyses [34,35,51].

Other investigators have analysed hydraulic fractures in matrix materials that deform plastically [55–57], poro-elastically [58–60], or by other mechanisms [38,61]. We recognize that deformation mechanisms other than elastic can be important, but this version of the analysis is limited to the simplest elastic behaviour.

Propagation

Fracture propagation is assumed to occur when the Mode I stress intensity equals the fracture toughness, $K_I = K_{Ic}$ [52]. This propagation criterion is widely used in linear elastic fracture mechanics, and it is a common assumption in models of hydraulic fracture propagation in rock [2,3,38,62], and soil [63–67]. Propagation is assumed to occur in quasi-static, mobile equilibrium, so displacements can be calculated with a static analysis. Fluid flow within the fracture limits the propagation velocity so dynamic effects can be ignored [68]. The fracture can only grow in the plane of the initial crack.

Implementing a solution to fluid flow and deformation

Implementing a solution to fluid flow and deformation requires discretizing equations representing three coupled processes, and then using an algorithm for solving simultaneous, non-linear equations. According to the conceptual model (Figure 1), change in pressure resulting from modest fluid injection or recovery will induce flow along the fracture and cause apertures to change. These processes are coupled because pressure and aperture affect both

continuity of fluid in the fracture (A1) and global displacement (C4) or (C7). However, flow in the fracture is also coupled to flow in the matrix, because q_L appears in (A1) and in the boundary condition (A12c). The latter two processes are further coupled because the global aperture (C4) or (C7) must equal the aperture resulting from asperity deformation (E1) or (E2), and this can only be satisfied by changes in effective stress.

Continued fluid injection could cause asperities to separate. This will first occur at some location along the fracture determined by comparing δ_o determined using (F1), or another suitable expression, to the current aperture. The effective stress must be zero wherever asperities separate, so $\sigma_e(x_1) = 0$ where $\delta(x_1) > \delta_o(x_1)$.

The stress intensity may have some finite value at the start of the problem if there is an initial aperture caused by opening of a crack. K_I increases during injection and propagation starts when $K_I = K_{Ic}$. When this occurs, it is assumed that the fracture is completely open and the effective stress on the fracture face is zero. Coupling between the global and local aperture calculations is not required when the fracture is completely open (i.e., they are automatically equal).

Discretization. The fracture and enveloping matrix are discretized using a rectangular grid (Figure 2(c)) with a variable spacing of M columns and N rows. The initial fracture lies along the lower row of the grid and is discretized into short segments. The matrix is discretized into blocks, and the width of individual columns of blocks are the same as the length of the segment in the adjacent fracture. The grid is node-centred, so all the calculations are taken at the centre of the blocks in the matrix or segments along the fracture. The grids are either cartesian or axisymmetric, depending on the geometry of the fracture, with x_1 along the rows and x_2 along the columns.

Coupled processes in static fractures. There are $(N+1)M$ unknowns in the system for a static fracture (not propagating). Fluid pressures (or heads) in the fracture and matrix represent NM unknowns. The effective stresses along the fracture provide another set of M unknowns. Therefore, there are $(N+1)M$ primary equations in this system, corresponding to NM fluid continuity equations and N equations matching displacements in the fracture (Table I). These are termed 'primary' equations because they are coupled and cannot be solved independently. An additional set of equations is used to solve for aperture, δ , fluid leakoff, q_L , and to couple the primary equations (Table I).

The primary equations include implicit finite difference forms (Table I) of the continuity equations in fracture (A1) and matrix (A11). Spatial derivatives in functions G and H , defined in (A1) and ((I) and (II)) in Table I, are written as centred differences in terms of h using (A2)–(A5) and (A13). The hydraulic conductivity in (A13) is weighted toward the upstream value to improve convergence when the porous media is partially saturated.

The other primary equation (III in Table I) requires that the aperture, which is determined based on global displacement of the fracture walls (C4) or (C7) due to the driving pressure (B1), is equal to the local aperture of a fracture resting on asperities, which is determined using (E1) or (E2). This is expressed in the first line in the third row of Table I. The second line ignores this primary equation when the effective stress is zero and the fracture is open. The third line is a 'penalty' function, which causes the primary function to produce a large value when the effective stress is negative. This is a computationally effective way to prevent effective stress from becoming negative.

Table I. Primary and coupling equations used in the analysis.

ID	Analysis	Number of equations
<i>Primary equation</i>		
I	$G(\delta\rho q) + \frac{\delta\rho - (\delta\rho)^{m-1}}{\Delta t} + \rho q_L = 0$ Continuity in the fracture (A1)	M
II	$H(\rho q) + S(h) \frac{h\rho - (h\rho)^{m-1}}{\Delta t} = 0$ Continuity in the matrix (A11)	$(N-1)M$
III	$\begin{aligned} (\delta_g - \delta_c)/\delta_g^* &= 0 & \text{if } (\sigma_e > \varepsilon) \text{ or } (\delta_p < \delta_o) \\ (\delta_g - \delta_c)/\delta_g^* &= 0 & \text{if } -\varepsilon < \sigma_e < \varepsilon \\ \Theta\sigma_e &= 0 & \text{if } \sigma_e < -\varepsilon \end{aligned}$ Matching local and global apertures	M
where ε is a small number (e.g. 10^{-10}) and Θ is a large number (eg. 10^{10})		
<i>Coupling equation</i>		
IV	$\delta_{g,\kappa}$ defined by (C4) for circular fracture $\delta_{g,\kappa}$ defined by (C7) for plane-strain fracture	M
V	$q_L = K_s \frac{h_f - h}{\Delta x_2}$ Fluid flux between fracture and matrix (A13)	M

The analysis uses the relations above with h and h_f written as dependent variables using equations given in the appendix. Nomenclature of symbols in Appendix I.

The system of primary equations is solved using Powell's hybrid [69] method implemented in the routine Hybrd1 in MINPACK [70]. Powell's hybrid method uses elements of both a modified Newton technique and the trust region method to find the zeros of a system of non-linear equations [69]. Hybrd1 converges when the relative error between the unknowns and the solution is estimated to be within a user-supplied tolerance value. Hybrd1 is relatively robust and accurate compared to other non-linear equation solvers used to solve a suite of benchmark problems by Dent *et al.* [71].

A solution is obtained by assuming initial conditions, boundary conditions, a time step, Δt , and a convergence tolerance. Hybrd1 calls a subroutine that first calculates the coupling equations using a current vector of estimates for the pressures and effective stresses, then it calculates the primary equations and returns a solution vector to Hybrd1. Values of the unknowns are adjusted until the error is less than a tolerance value (typically set between 10^{-8} and 10^{-5} in our calculations).

Failure to meet the convergence tolerance causes the time step, Δt , in the discretization of the continuity equation to be reduced to $1/n_1$ of the existing Δt . If Δt must be reduced, then it is increased by a factor of n_2 after Hybrd1 successfully converges for n_3 iterations. This allows the size of the time step to adapt in order to minimize execution time within a specified accuracy. The solution is marched through time by repeating this process, with changes in boundary conditions made as required to represent a particular problem. We typically used $n_1 = 3$, $n_2 = 2$, $n_3 = 4$.

Initial conditions. The analysis outlined above requires that computations start from equilibrium conditions. This is accomplished by specifying total confining pressure, initial pressure in the fracture, and the contact aperture distribution as in (F1). However, the aperture itself cannot be specified in advance because it depends on the effective stress distribution, which is initially unknown and must be determined to satisfy equilibrium. As a result, the initial distribution of aperture and effective stress must be calculated *before* the model is executed. This is done by finding the vector of σ_e that satisfies a system consisting of Equations III in Table I written at each segment along the fracture. Hybrd1 is used to solve for the unknown vector using the same approach outlined above.

Propagation. The approach to analysing propagation is to solve for pressures in the fracture and matrix, calculate the stress intensity, and then adjust P_{tip} and repeat the calculation of pressure and stress intensity until $K_I = K_{Ic}$. An iterative approach was used to find K_I such that

$$K_I = K_{Ic} \quad (1)$$

The total mass in the fracture, M_T , changes whenever P_{tip} is adjusted to satisfy $K_I = K_{Ic}$. The time step Δt from one fracture increment to the next must be adjusted during propagation to satisfy the global mass balance. This is accommodated by using

$$\Delta t = \frac{M_T^{m+1} - M_T^m}{Q\rho} \quad (2)$$

to adjust the time step during each iteration. This scheme assumes propagation only occurs during injection ($Q > 0$). The time step used during propagation is equal to the time step used in the discretization of continuity, unless the continuity time step has been cut to satisfy convergence (as described above). Details of the logic used during propagation are outlined in Appendix G.

EXAMPLES

The analysis outlined above is applicable to a wide range of problems involving injection or recovery of fluids from wells intersecting fractures. The analysis was formulated in a code called DFrx (Deformable Fracture), and the code was used to evaluate two example problems to illustrate possible applications.

Slug test

Slug tests are among the most widely used methods for characterizing the hydraulic conductivity of aquifers [72], and similar tests are also used to characterize oil reservoirs [11]. The test involves rapidly changing the hydraulic head in a well bore and monitoring the response as the aquifer or reservoir returns to equilibrium. The rate of change of storage in the well bore is equated with the flow rate into the aquifer or reservoir. Many analytical solutions have been proposed for estimating formation properties based on slug tests and most of them represent the formation as a porous layer, or perhaps as a dual-porosity layer [16,17].

A major shortcoming of slug tests is that the pressure signal they produce is only weakly sensitive to the storage properties of the formation. One possibility for reducing this shortcoming is to measure axial displacement of a well bore during a slug test and then analysing the displacement signal to estimate storage properties. It is possible to measure such displacements [73,74], and the model outlined above can be used to predict this response in fractured formations.

Analysis. Slug tests were analysed by configuring the code to use the boundary condition given in (A7) and (A8), and parameters selected to represent conditions at depths of several tens of meters in fractured gneiss, typical of rock in the vicinity of Clemson, South Carolina. The matrix was assumed to be impermeable for the initial evaluation. The fracture was assumed to be circular with a radius of 500 m (large enough so the edge has no effect) with a confining stress equivalent to a depth of 30 m (Figure 3). The effect of the free surface was ignored to illustrate the model capability. A free surface could be included using the approach described by Murdoch [67].

The fracture was divided into 65 grid segments whose size increased with distance from the well. The slug was assumed to be $h_o = 2$ m of head, and the radius of the boring and casing was $r_w = r_c = 0.076$ m. Young's modulus, $E = 40$ GPa, and initial normal stiffness, $K_{ni} = 10^9$ Pa/m, to approximately represent gneiss (Table II).

The contact aperture of the fracture was assumed to be $\delta_o = 400$ μm , but the actual aperture of the mouth of the fracture reduced to $\delta = 236$ μm using the combination of confining stress and initial pressure selected to represent the problem (Table II). The Bandis *et al.* [54] model (E1) for local deformation of asperities was used, and this causes the effective normal stiffness to increase with effective stress. Storativity of a confined aquifer is approximately related to the normal stiffness of the fracture. A storativity of $S = 1.2 \times 10^{-5}$ was calculated from the effective normal stiffness under the assumed conditions.

The slug test itself was simulated by specifying the hydraulic head (as in Equation (A8)) in the well as a linearly increasing function of time ($dh/dt = 0.5$ m/s) for $t \leq 4$ s, and then changing the boundary condition to include borehole storage (Equation (A7b)) after $t > 4$ s. This rate of pressurization is representative of field conditions, and it provides a realistic start to the

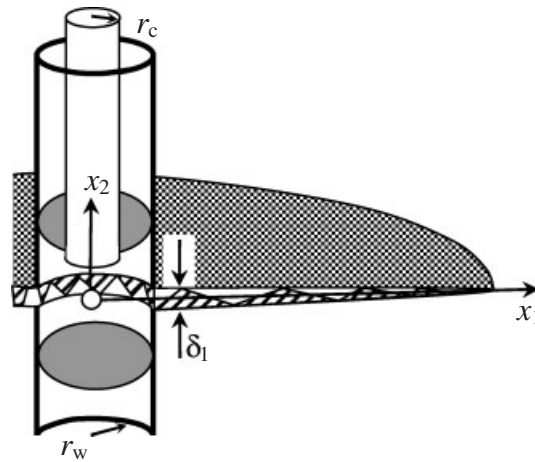


Figure 3. Flat-lying, axisymmetric, asperity-supported fracture isolated by straddle packer in a well. Configuration assumed for slug test analysis.

Table II. Parameters used in the slug test analysis.

E	40 GPa	α	1.0
ν	0.3	P_c	2.9×10^5 Pa
K_{Ic}	$1.0 \text{ MPa m}^{1/2}$	S_s	10^{-6} m^{-1}
a_i	550 m	σ_c	5.8×10^5 Pa
K_{sat}	10^{-25} m/s	K_{ni}	10^9 Pa/m
σ_{ec}	2.4×10^4 Pa	$\delta_{o,con}$	$4 \times 10^{-4} \text{ m}$
		$P_{initial}$	-3.0×10^4 Pa

simulation compared to the instantaneous increase in head assumed in most analytical solutions.

Results. Initial tests were conducted to verify the DFrX output by comparing results to an analytical solution given by Cooper *et al.* [75]. Sixty time steps were used for the simulations and run times were approximately 2 min using a convergence tolerance of 10^{-10} (Pentium 4, 2, 8 GHz, 1GB RAM). The code is capable of automatically adjusting the size of time steps, but no such adjustments were required for this problem.

Several dozen simulations were conducted to verify that the time scaling in the numerical model was the same as in the analytical model. A variety of different initial apertures were used, for example, and all the results resolved to essentially single curve when plotted using

$$t_d = \frac{tT}{r_c^2} \quad (3)$$

as the time axis [74], where the effective transmissivity of the fracture is

$$T = \frac{\delta_1^3 \gamma}{12\mu} \quad (4)$$

with δ_1 the aperture at the mouth of the fracture.

Normalized hydraulic head from the numerical analysis is similar to results from the analytical solution (Figure 4), with relative errors of 0.01 or less. The pressurization time is assumed to be instantaneous in the analytical solution, so it is ignored in the numerical results used for comparison in Figure 4. Storage in the fracture will depend on both the effective normal stiffness and on the global deformation of the fracture, which is controlled by the elastic modulus and fracture length. The value of storativity calculated from the normal stiffness alone gives results that are similar to the Cooper *et al.* [75] solution, suggesting that the global stiffness of the fracture plays a minor role in this example.

Results intended to represent field conditions (Table II) show the hydraulic head and displacement increase during initial pressurization, but then the hydraulic head begins to fall immediately while the fracture continues to dilate (increasing displacement). The displacement reaches a maximum of 1.6 μm approximately 30 s after the peak pressure (Figure 5). As a result, the relationship between hydraulic head and displacement shows hysteresis (Figure 6). Similar hysteretic responses are observed during slug tests in boreholes fitted with extensometers [73,74].

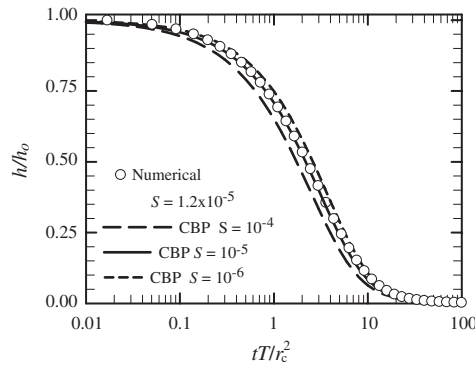


Figure 4. Normalized hydraulic head as a function of dimensionless time for numerical results (points) and analytical solution by Cooper *et al.* [75] (lines).

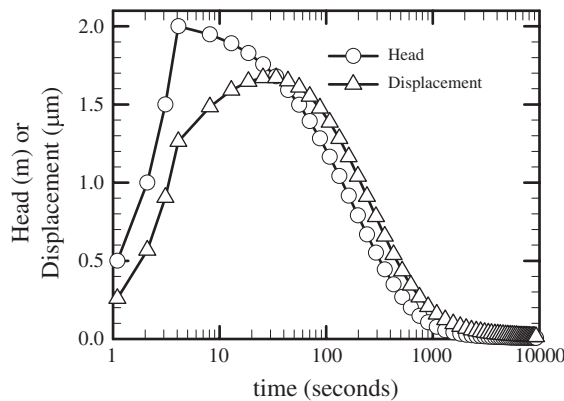


Figure 5. Hydraulic head in a well and displacement normal to fracture during slug test.

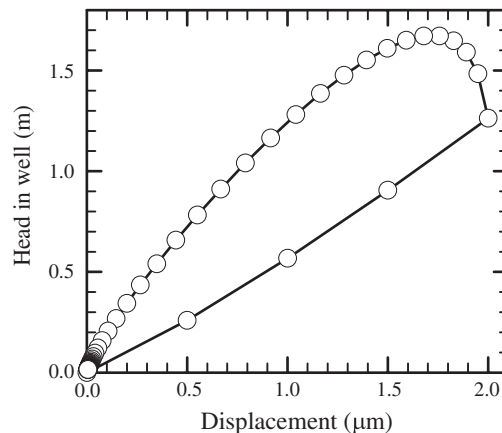


Figure 6. Hydraulic head in a well as a function of displacement normal to fracture during slug test.

Even though the analytical solution and the numerical results are similar, the analytical solution would predict displacements of the borehole walls that are directly proportional to the head. As a result, the displacement curve in Figure 5 would have the same shape as the pressure curve, and the curve in Figure 6 would reduce to a single line, losing the effect of hysteresis. The results of our analysis better represent field measurements of displacements and suggest that one application for the analysis could be to help interpret slug tests in fractured formations.

Propagation and closure of a hydraulic fracture

Hydraulic fractures are widely used for estimating *in situ* stresses. Wellhead pressures are evaluated as a function of time after injection has been terminated in an effort to estimate the state of the fracture. The pressure at the moment a fracture closes is widely accepted as the minimum confining stress acting normal to the fracture [6]. Recent experiments have shown that in some cases fractures could close at pressures that differ from the confining stress, a finding that is at odds with some stress testing interpretations [76]. Recent analyses of the process of hydraulic fracture closure (e.g. References [76–78]) have assumed uniform pressure and effective stress in the fracture, and have used simplified analyses of leakoff. It seems reasonable to expect that flow within a hydraulic fracture during closure will affect the pressure log, so the approach described above could improve interpretations of stress tests and explanations of laboratory tests.

Most applications of hydraulic fractures for stress testing have been done at relatively great depths in rock, but some applications have used fractures at relatively shallow depths in soil [63–65, 79–81]. The shallow applications can be used directly to estimate stresses for geotechnical or environmental applications, or they can be used as analogs for processes that occur in rock at higher stresses, conditions that are more difficult to simulate experimentally. For example, the behaviour of hydraulic fractures in partially saturated silty clay appears to be similar to the linear elastic behaviour commonly used to represent fractures in rock [63–67]. Malin [81] created hydraulic fractures in the laboratory and field at depths of several meters in an effort to estimate *in situ* stresses, and we used the conditions of his experiments for the example here.

Analysis. An analysis was configured by assuming a vertical, rectangular fracture is created by injecting water at a constant rate into a narrow slot (Figure 7), conditions that represent Malin's experiments. Fluid properties for water at standard conditions were used and wall friction in the fracture was ignored. A grid with variable spaced rows and columns was used to represent the fracture and partially saturated matrix. The enveloping matrix was assumed to be homogeneous, partially saturated soil and characterized by parameters in Table III.

Results. The example simulation required 138 time steps, where $\Delta t = 1$ s after pumping had stopped. A convergence criterion of 10^{-6} was used. The time increment was automatically reduced and increased during roughly half of the time steps, and this typically was required when grid blocks in the matrix approached saturation. The global mass balance error during propagation was in the range of 0.005–0.08, and during closure it was less than 0.002. The relatively high mass balance error during propagation seemed acceptable because our main interest was in simulating closure. The mass balance error during propagation can be reduced by using a finer finite difference grid (Figure 2(c)).

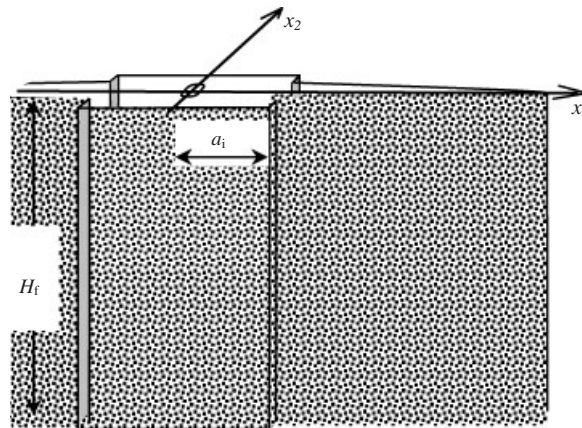


Figure 7. Rectangular, plane-strain hydraulic fracture propagating from a starter slot. Left-side of fracture is truncated.

Table III. Parameters used in the hydraulic fracturing analysis.

E	40 MPa	α	1.0
ν	0.3	P_e	100 Pa
K_{Ic}	$0.04 \text{ MPa m}^{1/2}$	S_s	10^{-6} m^{-1}
a_i	0.01 m	σ_c	$3.56 \times 10^4 \text{ Pa}$
δ_{slot}	0.001 m	K_{ni}	10^8 Pa
Q	$3.0\text{E-}7 \text{ m}^3/\text{s}$	$\delta_{o,\text{con}}$	$3 \times 10^{-4} \text{ m}$
K_{sat}	$3.0\text{E-}9 \text{ m/s}$	P_{initial}	$-3.0 \times 10^4 \text{ Pa}$
n	1.23	σ_{ec}	$2.4 \times 10^4 \text{ Pa}$
α_v	1.0	H_f	10 cm
θ_{sat}	0.5		
θ_r	0.1		

The fracture grew from a half length of 0.01 m to approximately 0.1 m during the first 44 s, and then the fracture closed for the next 80 s, according to the simulation (Figure 8). Fluid leaked into the partially saturated material during injection and the water content of the matrix adjacent to the fracture increased as leakoff continued during closure (Figure 8). Injection pressure increased sharply until propagation started after 0.8 s. The pressure decreased to roughly 1.1×10^5 Pa at the end of injection, and the aperture increased from 1 mm (the width of the initial slot) to 1.7 mm (Figure 9). There was a slight decrease in pressure when the pump was turned off in the simulation, and then both the pressure and aperture decreased fairly steadily until 120 s, when the pressure decreased abruptly and then became roughly constant at approximately -100 Pa (Figure 9).

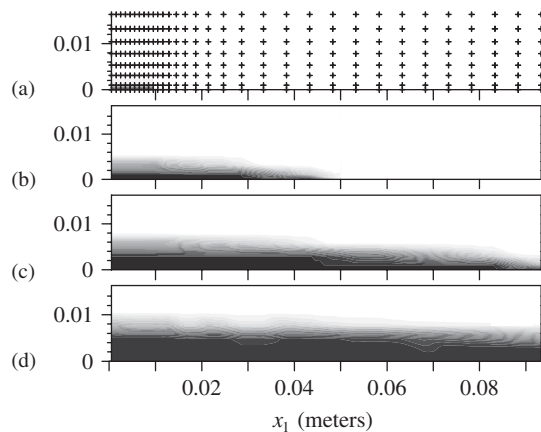


Figure 8. Cross-section showing water content in matrix adjacent to hydraulic fracture in soil that is partially saturated: (a) conditions after 1 s of injection prior to propagation, showing grid; (b) during propagation; (c) at the end of injection (44 s); and (d) end of run (120 s).

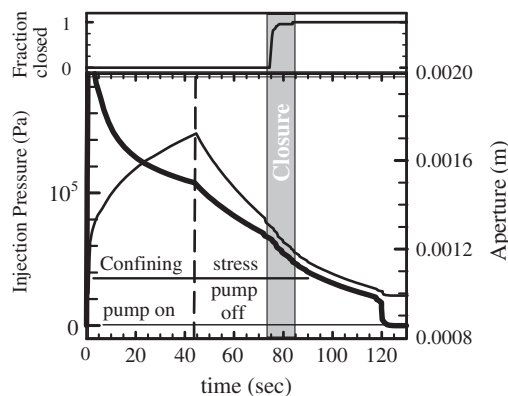


Figure 9. Injection pressure and aperture at the mouth of a hydraulic fracture during and following injection. Closing of fracture to rest on asperities indicated by upper plot and grey bar.

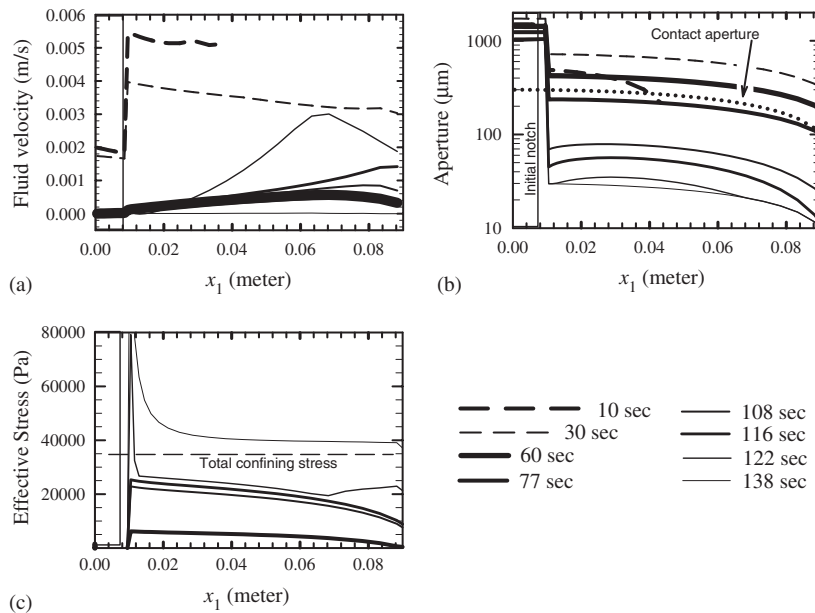


Figure 10. Profiles of: (a) fluid velocity in fracture; (b) aperture; and (c) effective stress along the half-length of a fracture at different times.

Asperities on the fracture surface first came in contact at approximately $t = 74$ s when the injection pressure was approximately 6.5×10^4 Pa (Figure 9). The initial contact occurred at the edge of the initial slot in this simulation because of the distribution of δ_o given by Equation (32). In this case, initial contact progressed from the edge of the slot to the fracture tip and the entire fracture was resting on asperities at $t = 85$ s (Figure 10(b)). The fluid pressure was 4.5×10^4 Pa when the fracture was fully resting on asperities (Figures 9 and 10(b)).

The closure process is manifested by a subtle change in the pressure log. The slope steepens when asperities first make contact, and it flattens slightly when the fracture is fully resting on asperities. The pressure log varies smoothly during most of the simulation, but it is characterized by slight downward steps when the asperities first make contact (Figure 9).

A much more striking change in the pressure log occurs later, at 120 s, when the pressure drops suddenly (Figure 9). This occurs when the effective stress exceeds σ_{ec} , (Appendix I) and the deformation of the asperities changes according to (E2). Essentially the change in deformation amounts to a shift from constant asperity stiffness, to a stiffness that increases with σ_e . The relationship between effective stress and normal stiffness apparently plays an important role in the form of the pressure log.

The analysis suggests that fluid continues to flow within the fracture during closure. Fluid velocity drops by roughly a factor of 10 when the pump is turned off, but it continues to flow in response to an increase in the leakoff rate toward the tip (Figure 10(a)). The fluid velocity actually increases near the tip as the deformation of asperities changes when $\sigma_e = \sigma_{ec}$ at 122 s. This change in velocity results from an increase in the head gradient near the tip (not shown) in response to the stiffening of the asperities.

The contact aperture is assumed to increase with increasing distance from the tip, and this affects the aperture during closure because it causes asperities to first come in contact at the end of the initial notch (Figure 10(b)). The fracture continues to close after the asperities make contact, but the aperture becomes particularly narrow adjacent to the end of the notch. This suggests the closure process could create a restriction to flow between the well and the fracture (Figure 10(b)). Interestingly, a similar displacement field is recognized to occur where hydraulic fractures intersect boreholes (Reference [82, Figures 6–19]).

The effective stress is zero during propagation and shortly after the pump is turned off, but σ_e increases when the asperities make contact (Figure 10(c)). Effective stress is greatest near the initial notch because the contact aperture, δ_o , is greatest there according to (F1). Effective stress increases sharply adjacent to the notch near the end of the simulation as the deformation of the asperities changes when $\sigma_e > \sigma_{cc}$. The final distribution of σ_e exceeds the confining stress mostly because excess effective stress is required to create the residual aperture at the end of the simulation (Figure 10(b)). The effective stress exceeds σ_c also because the fluid pressure has become negative at the end of the simulation. This low fluid pressure occurs because the pore pressure in the matrix is negative, which is typical of conditions in the vadose zone.

DISCUSSION

In situ stresses are commonly estimated graphically using various transforms to highlight characteristic signatures on pressure decay logs that are believed to indicate fracture closure [6]. Recent experimental results [76] suggest that this approach could be subject to errors because fractures with leakoff can close at pressures that differ from the confining stress, and these pressures could be difficult to identify as signatures on pressure logs. Malin [81] also found that using graphical methods to interpret pressure logs from hydraulic fractures created in the vadose zone can produce ambiguous results.

The example shown here confirms those experimental results by simulating details of the closure process. The results show that a fracture can close to rest on asperities over a range of pressures that *exceed* the confining stress, similar to the interpretation of experimental results reported by van Dam *et al.* [76, Figure 7]. The most striking change in the simulated pressure log occurs at 120 s (Figure 9). This change in the log occurs after the fracture has closed and the pressure has dropped below the confining stress, and is a response to the deformation style of the asperities assumed for this example (Figure 9). This type of material response by asperities might never occur in nature, but it points out the importance that progressive deformation of asperities has on the form of the pressure decay log.

Graphical methods of interpreting the pressure decay log to estimate *in situ* stress would have difficulties with the example shown here, and with the results of experiments reported by van Dam *et al.* [76]. The subtle change in the pressure log during closure probably could be detected using a graphical interpretation, but the inferred stress would be *greater* than the confining stress. The striking change at the end of the log could also have been interpreted to be a result of fracture closure, but this change occurs at *less* than the confining stress.

In addition to analysing stress tests, the contact aperture (F1) can be interpreted as the thickness of proppant in a fracture. It seems possible that this analytical approach can be used to evaluate pressure records from hydraulic fracturing operations in order to estimate proppant distribution.

One possible application for the analysis described above is to interpret the results of hydraulic fracturing stress tests more rigorously than was possible using graphical methods or analytical solutions. Gulrajani and Nolte [78] describe the state-of-the-art in using analytical solutions to interpret fracturing pressure logs and they recognize possible limitations that result from the assumptions required to obtain those solutions. They suggest that ‘an appropriately calibrated numerical simulator that adequately simulates the important processes during a fracturing application’, might add insights, but they do not identify a particular simulator that meets these specifications. Gulrajani and Nolte [78] also emphasize the need to apply non-linear, parameter estimation methods when using numerical simulators and they recognize potential pitfalls associated with these computationally intensive techniques.

The analysis outlined here is simpler than research fracturing codes and probably will execute faster than those codes, but it can represent more processes than analytical solutions. The analyses shown in Figures 8–10 required approximately 8 min of CPU time on a 2.8 GHz Pentium 4 computer (1 GB RAM). As a result of this relatively short execution time, it is practical to adapt the code for applications involving parameter estimation. DFRx has been interfaced with parameter estimation routines that use implicit filtering [83] and the Levenberg–Marquardt routine [84]. It has also been implemented with the commercial, parameter-estimation software PEST.

The code can be readily adapted to include other fluid and material properties and processes. For example, the current analyses assumes Newtonian fluid is injected into the fracture, however, it is to straightforwardly include other fluid rheologies by modifying the flow laws in (A3) and (A13). Simple functions were used for local displacements due to deformation of asperities (E1 and E2), but other constitutive relations can readily be included pending justification by lab experiments or other methods. A simple distribution of contact aperture (F1) was assumed for the examples given here because little is known about this distribution in the field. Other simple distributions of contact aperture (uniform distribution, for example) were tested and solutions could readily be obtained for these cases. Propagation criteria that differ from the one used here could be appropriate for hydraulic fractures in some materials, such as cohesionless sediments [57,85].

CONCLUSIONS

Fluid flow in the vicinity of wells intersecting deformable fractures is important to a wide range of problems, and a new model and code have been developed for analysing relevant aspects of these problems. Our model differs from existing analyses in that it considers both fractures that are asperity-supported and at rest, and fractures that are fully open and propagating. Moreover, the analysis can include transitions between the two conditions, so it can simulate the opening, propagation, and closing of a fracture, for example. This is accomplished by using a term called the contact aperture, which is the aperture where asperities on a closing fracture surface first make contact. Contact aperture varies over a fracture surface, and the distribution of this parameter allows the code to distinguish regions that are open from those that are asperity supported.

The closing of an open fracture is assumed to produce an effective stress as the fracture face becomes partially supported by asperities. The analysis includes effective stress on the fracture face as an unknown, which is determined by requiring that global displacements of the fracture

walls determined from an elasticity solution match the local displacements of asperities determined from expressions based on lab experiments. Global displacements depend on both the fluid pressure in the fracture and the effective stress, whereas asperity deformation depends only on effective stress. This requirement introduces a non-linear mechanical interaction between fluid pressure, effective stress and aperture for asperity-supported fractures.

The code uses analytical expressions to determine displacements, so meaningful problems can be solved relatively quickly. The execution times are fast enough so the inversion of data from well tests or hydraulic fracturing tests can be accomplished in practical times.

APPENDIX A: FLUID FLOW

A.1. Continuity of mass in the fracture

Continuity of mass in the fracture gives [68]

$$\begin{aligned} \frac{\partial(\rho_f \delta)}{\partial t} + \rho_f q_L &= 0 \\ G &= \frac{\partial(\rho_f q \delta)}{\partial x_1} + \frac{\rho_f q \delta}{x_1} \kappa \\ \kappa &= \begin{cases} 0 & \text{plane strain} \\ 1 & \text{axisymmetric} \end{cases} \end{aligned} \quad (\text{A1})$$

where δ is the fracture aperture, ρ_f is fluid density, q is the volumetric flux or average velocity within the fracture, and q_L is the volumetric flux out through the walls of the fracture.

The problems considered here use liquids in the fracture, so the fluid density is given by (e.g. Reference [86])

$$\rho_f = \rho_o e^{\beta(P-P_o)} \quad (\text{A2})$$

The fluid flux is assumed to be given by the parallel plate approximation [87]

$$q = -\frac{\delta^2 \gamma}{12\mu} C_f \left(\frac{\partial h_f}{\partial x_1} \right) \quad (\text{A3})$$

where the compressibility of the fluid is assumed to be constant across the width of the fracture. Here C_f is a friction coefficient that accounts for roughness of the fracture walls and the tortuosity of flow paths through a partially open crack. A variety of approaches have been suggested for determining a friction coefficient within the range $0 < C_f < 1.0$ [49,50]. The method used here is to account for tortuosity using

$$C_f = \frac{\alpha}{2 - \alpha} \quad (\text{A4})$$

where α is the ratio of the area of open pore space in the fracture to the total area of the fracture surface [48,88,89]. Additional terms can be used to account for the roughness of the fracture walls [50,87].

It seems likely that α , and thus C_f , change progressively during normal displacement of a fracture [89]. Changes in effective stress are small for the examples we have evaluated, so we have assumed that C_f is constant and given by (A4) where asperities are in contact, and $C_f = 1.0$

where the fracture is open. Other schemes where C_f changes as a linear, or some other, function of effective stress can be easily implemented in the model.

Relations that involve fluid flow are written in terms of hydraulic head, h , whereas those that involve multiphase properties or mechanical displacements are written in terms of fluid pressure, P . They are related using

$$h = \frac{P}{\rho_f g} + z \quad (\text{A5})$$

where z is vertical distance from a horizontal reference plane.

Boundary conditions for (A1) depend on interactions between the fracture and the well at $x_1 = r_w$, and whether the fracture is propagating at $x_1 = a$.

Flow rate at fracture mouth known. When the volumetric injection rate Q into the fracture is known, the boundary condition at the mouth of the fracture is

$$q_{\text{well}} = \frac{Q}{\delta_1 L} \quad \text{at } x_1 = r_w \quad (\text{A6})$$

where δ_1 is the aperture at the well, $L = 2\pi r_w$ for a circular fracture and $L = H_f$ is the effective fracture height for a plane-strain fracture.

The volumetric flow rate into a fracture, Q , can be affected by changes in wellbore storage. A mass balance on the well bore requires that

$$Q = Q_{\text{pi}} - \frac{1}{\rho_f} \frac{\partial(\rho V_s)}{\partial t} \quad (\text{A7a})$$

where V_s is the volume of fluid stored in the wellbore or pumping system outside of the fracture, and Q_{pi} is the volumetric rate at which fluid is pumped into the well. During a slug test or the recovery phase following a constant rate test in an open well, for example, $Q_{\text{pi}} = 0$, and for an open vertical well $V_s = \pi r_w^2 h_w$, so

$$Q = -\pi r_c^2 \frac{\partial h_w}{\partial t} \quad (\text{A7b})$$

where h_w is the hydraulic head in the well bore, r_c is the radius of the well casing, and changes in fluid density are ignored (ρ_f is constant).

During some well tests, Q_{pi} is typically constant at the wellhead, but the volume of fluid stored in the wellbore might change with pressure due to compliance of the pumping system, dV_s/dP , and fluid compressibility, β . This could occur during hydraulic fracturing tests or pressure pulse tests where intervals of a borehole are isolated by packers. It follows that

$$Q = Q_{\text{pi}} - \left(\frac{1}{\rho_f} \frac{\partial(\rho_f V_s)}{\partial P} + \beta V_s \right) \frac{\partial P_w}{\partial t} \quad (\text{A7c})$$

In pumping systems that contain small volumes of gas, V_g , the compressibility of the gas can be more important than the compliance of the pump and tubing. Assuming the injection tubing is

rigid and the gas behaves ideally, then

$$Q = Q_{pi} - \left(V_g P_a \frac{1 - \beta(P_a + P)}{(P_a + P)^2} + \beta V_s \right) \frac{\partial P_w}{\partial t} \quad (\text{A7d})$$

In some cases, even in the absence of gas, fluid compressibility can drive fracture propagation [90], but this effect is small and has been ignored here.

Pressure at fracture mouth known. Some well tests maintain a constant pressure, whereas others require that the pressure varying according to a specified history (e.g. the pressure increase at the start of a slug test). The boundary condition at the mouth of the fracture in this case is

$$P_w = P_s \quad \text{at } x_1 = r_w \quad (\text{A8})$$

Fracture tip (no propagation). No-flow conditions are assumed at the tip of a static fracture, so

$$\frac{\partial P}{\partial x_1} = 0 \quad \text{at } x_1 = a \quad (\text{A9})$$

Fracture tip (propagation). The boundary condition that should be used to properly represent the physics of flow at the fracture tip has drawn considerable attention and the issue remains unresolved. One approach is to use an analytical solution to idealize conditions at the tip of a hydraulic fracture for the boundary condition in a more general numerical model, as was done by Desroches and Carter [91]. This type of solution is available for a few end-member tip conditions (e.g. References [45,92,93]). However, other factors, such as mode III branching or bridging, introduce additional fracture tip scales that are difficult to quantify at present, yet the interplay between these scales could be a critical factor affecting the final fracture geometry, orientation, and pressure distribution.

We recognize the importance of specifying a mathematically consistent tip boundary condition, but we already included a variety of processes (Darcy leakoff, fracture roughness) that go beyond the available asymptotic analyses of tip conditions. As a result, the application of existing asymptotic analyses to our model is unclear. Therefore, we chose as the boundary condition to specify the pressure at the tip

$$P = P_{tip} \quad \text{at } x_1 = a \quad (\text{A10})$$

i.e. at the last grid block in the finite difference approximation used for fluid flow.

The boundary condition in (A10) facilitates the analysis of fluid pressure within the fracture and adjusting P_{tip} provides a convenient mechanism for satisfying the propagation criterion.

Continuity in matrix

Continuity of mass in the matrix gives

$$H + \frac{\partial \theta}{\partial h} \frac{\partial(\rho h)}{\partial t} = 0$$

$$H = \frac{\partial(\rho_f q_1)}{\partial x_1} + \frac{\partial(\rho_f q_2)}{\partial x_2} + \frac{\rho_f q_1}{x_1} \kappa \quad (\text{A11})$$

$$\kappa = \begin{cases} 0 & \text{plane strain} \\ 1 & \text{axisymmetric} \end{cases}$$

Fluid density was assumed to be constant in partially saturated conditions.

Boundary conditions used with (A11) include

$$q_1(0, 0 < x_2 < x_{2 \max}) = 0 \quad (\text{A12a})$$

$$q_1(x_{1 \max}, 0 < x_2 < x_{2 \max}) = 0 \quad (\text{A12b})$$

$$q_2(0 < x_1 < x_{1 \max}, 0) = q_L(0 < x_1 < x_{1 \max}) \quad (\text{A12c})$$

$$h(0 < x_1 < x_{1 \max}, x_{2 \max}) = h_o \quad (\text{A12d})$$

where $x_{1 \max}$ and $x_{2 \max}$ are boundaries of the flow domain ($x_{1 \max} = a$ in our simulations).

Volumetric flux within the matrix is determined by Darcy's Law

$$q_n = -K_n \frac{\partial h}{\partial x_n}, \quad n = 1, 2 \quad (\text{A13})$$

Leakoff flux, q_L , is calculated using a finite difference form of (A13) at the wall of the fracture.

Water saturation in the matrix is assumed to be arbitrary to facilitate analysing fracture propagation in the vadose zone. The volumetric water content in the matrix, θ , is assumed to be a function of pore pressure. We used a function based on Reference [94], but other functions are also available. Our model uses

$$\theta = \theta_r + (\theta_s - \theta_r) \left[\frac{1}{1 + (\alpha_v |P - P_e|)^n} \right]^{(n-1)/n} + PS_s \quad \text{where } P < P_e \quad (\text{A14a})$$

$$\theta = \theta_s + S_s P \quad \text{where } P \geq P_e \quad (\text{A14b})$$

where P_e is the air-entry pressure. The specific storage, S_s , is assumed to be constant at all saturations. The hydraulic conductivity of the matrix follows from (A14a) as [94]

$$K = K_s \quad \text{where } P \geq P_e \quad (\text{A15a})$$

$$K = K_s \left(\frac{1}{1 + (\alpha_v |P - P_e|)^n} \right)^{(n-1)/2n} \left\{ 1 - \left(\frac{(\alpha_v |P - P_e|)^n}{1 + (\alpha_v |P - P_e|)^n} \right)^{(n-1)/n} \right\}^2 \quad \text{where } P < P_e \quad (\text{A15b})$$

APPENDIX B: DRIVING PRESSURE

A fracture resting on asperities will be held open by the internal fluid pressure, P , and in part by the effective stress acting on the asperities, σ_e . The driving pressure for the crack is

$$P_d = \alpha P + \sigma_e - \sigma_c \quad (\text{B1})$$

A force balance indicates that α is ratio of the area of open space to total fracture surface, the same definition used to characterize tortuosity in (A4). This definition of driving pressure allows us to use elastic displacement equations to determine apertures of fractures that are resting on asperities, as well as those that are fully open. The effective stress is zero when the fracture is fully open or propagating, so for this case the driving pressure reduces to the familiar form

$$P_d = P - \sigma_c \quad (\text{B2})$$

APPENDIX C: GLOBAL DISPLACEMENTS AND APERTURE

Fracture aperture is determined by assuming P_d is uniformly distributed over each segment, although it varies over the entire fracture. For an analysis considering a segment spanning $b \leq x_1 \leq c$, the driving pressure is

$$P_{d1}(x) = \begin{cases} P_d, & b \leq x_1 \leq c \\ 0, & 0 < x_1 < b \text{ or } c < x_1 < a \end{cases} \quad (\text{C1})$$

Defining for convenience

$$\begin{aligned} \rho &= x_1/a \\ b^* &= b/a \\ c^* &= c/a \\ C_1 &= \frac{4a(1-\nu^2)}{\pi E} \end{aligned} \quad (\text{C2})$$

The aperture of a plane-strain fracture loaded by driving pressure P_d uniformly distributed over a patch that spans the interval $b < x_1 < c$ is [95, p. 5.12].

$$\begin{aligned} \delta_p(x_1, b^*, c^*, P_d) &= C_1[A - B + C]P_d \\ A &= (c^* - \rho) \cosh^{-1} \frac{1 - c^*\rho}{|\rho - c^*|} \\ B &= (b^* - \rho) \cosh^{-1} \frac{1 - b^*\rho}{|\rho - b^*|} \\ C &= \sqrt{1 - \rho^2}(\sin^{-1} c^* - \sin^{-1} b^*) \end{aligned} \quad (\text{C3})$$

The total global aperture of a plane-strain fracture is obtained by superposition of the displacements due to driving pressures at each of the finite difference grid blocks

$$\delta_g(\rho, P_d) = \sum_{i=1}^m \delta_p(\rho, b_i^*, c_i^*, P_{di}) \quad (\text{C4})$$

An equivalent solution for a circular fracture can be obtained from Reference [96, p. 489]

$$\delta_p(\rho) = 2C_1 \int_{\rho}^1 \frac{\mu}{(\mu^2 - \rho^2)} d\mu \int_0^1 \frac{\tau P_d(\tau \mu a)}{\sqrt{1 - \tau^2}} d\tau \quad (\text{C5})$$

which gives the aperture of a circular fracture with P_d an arbitrary function of ρ . Assuming the driving pressure is uniformly distributed over an annular patch as in (C1) and performing the necessary integration in (C5) gives

$$\delta_p(\rho, b^*, c^*, P_d) = C_1 [D(b^*, \rho) - D(c^*, \rho)] P_d \quad \text{for } c^* < \rho < 1 \quad (\text{C6a})$$

$$\delta_p(\rho, b^*, c^*, P_d) = C_1 [D(b^*, \rho) - G(c^*, \rho)] P_d \quad \text{for } b^* < \rho < c^* \quad (\text{C6b})$$

$$\delta_p(\rho, b^*, c^*, P_d) = C_1 [G(b^*, \rho) - G(c^*, \rho)] P_d \quad \text{for } 0 < \rho < b^* \quad (\text{C6c})$$

with

$$D(\xi, \rho) = \int_{\rho}^1 \sqrt{\frac{\mu^2 - \xi^2}{\mu^2 - \rho^2}} d\mu = \frac{\rho^2 - \xi^2}{\rho} F(u_1, t_1) - \rho E(u_1, t_1) + \varphi_1$$

$$\varphi_1 = \sqrt{\frac{1 - \rho^2}{1 - \xi^2}} \quad (\text{C6d})$$

$$u_1 = \sin^{-1} \varphi_1$$

$$t_1 = \frac{\xi}{\rho}$$

and

$$G(\xi, \rho) = \int_{\xi}^1 \sqrt{\frac{\mu^2 - \xi^2}{\mu^2 - \rho^2}} d\mu = \varphi_2 - \xi E(u_2, t_2)$$

$$\varphi_2 = \sqrt{\frac{1 - \xi^2}{1 - \rho^2}} \quad (\text{C6e})$$

$$u_2 = \sin^{-1} \varphi_2$$

$$t_2 = \frac{\rho}{\xi}$$

where $F(u,t)$ and $E(u,t)$ are the elliptic integrals of the first and second kind, respectively [97]. The total aperture of the crack is

$$\delta_g(\rho, P_d) = \sum_{i=1}^m \delta_p(\rho, b_i^*, c_i^*, P_{di}) \quad (C7)$$

APPENDIX D: STRESS INTENSITY FACTORS

The total Mode I stress intensity is obtained by superimposing solutions for driving pressures applied to patches on the crack face, using the same approach as the aperture calculations. The Mode I stress intensity for a plane-strain crack loaded by P_d applied over $b < x_1 < c$ is given by Tada *et al.* [95, 5.12]

$$K_I = \frac{P_d \sqrt{a}}{\sqrt{\pi}} [\sin^{-1} c^* - \sin^{-1} b^* \pm (\sqrt{1 - c^{*2}} - \sqrt{1 - b^{*2}})] \quad (D1)$$

The plane-strain crack is centred on $x_1 = 0$ and K_I is taken to apply to the positive x_1 side. For this case, the \pm is $-$ when $b^* > 0$ and it is $+$ when $c^* < 0$. Loading on the crack is assumed to be symmetric about the x_2 -axis for this work, but loads on the entire crack ($-a < x_1 < a$) contribute to K_I and are considered. It follows that the total Mode I stress intensity factor is

$$K_I = \sum_{i=-m}^m (K_I)_i \quad (D2)$$

where negative values of i indicate negative values of b^* and c^* .

For a circular crack, K_I for P_d applied over $b < x_1 < c$ can be obtained by integrating 24.5 in Reference [95] to give

$$K_I = \frac{2P_d \sqrt{a}}{\sqrt{\pi}} \int_{b^*}^{c^*} \frac{\xi}{\sqrt{a^2 - \xi^2}} d\xi = \frac{2P_d \sqrt{a}}{\sqrt{\pi}} (\sqrt{1 - b^{*2}} - \sqrt{1 - c^{*2}}) \quad (D3)$$

and the total stress intensity is again

$$K_I = \sum_{i=-m}^m (K_I)_i \quad (D4)$$

APPENDIX E: LOCAL DISPLACEMENTS AND FRACTURE NORMAL STIFFNESS

Asperities that hold open a fracture at depth are assumed to deform as the effective stress changes when fluid pressures change. Deformation of asperities will in turn lead to changes of aperture. Both lab experiments [54] and theoretical analyses [34,35,98] indicate that the aperture decreases roughly in proportion to increases in effective stress when the changes in effective stress is relatively modest. However, the aperture diminishes to some minimum finite value, δ_{\min} , when effective stress becomes large. A variety of relations between aperture of an asperity-supported fracture and effective stress have been proposed (review by Zimmerman and Main [50]), but functionally they are subtle variations of a linear closure that becomes asymptotic at

high effective stress. Two relations have been used in the analysis here. One is a common form suggested by Bandis *et al.* [54]

$$\delta_c = \delta_o - \frac{(\delta_o - \delta_{\min})\sigma_e}{K_{ni}(\delta_o - \delta_{\min}) + \sigma_e} \quad (\text{E1})$$

Many applications of the flow through fractures supported by asperities consider changes in fluid pressure that are small, and the aperture is nearly a linear function of effective stress. We suggest an alternative function

$$\delta_c = \begin{cases} \delta_o - \frac{\sigma_e}{K_{ni}}, & \sigma_e \leq \sigma_{ec} \\ \left(\delta_o - \frac{\sigma_{ec}}{K_{ni}} - \delta_{\min} \right) e^{-(\sigma_e - \sigma_{ec})/K_{ni}(\delta_o - \delta_{\min}) - \sigma_{ec}} + \delta_{\min}, & \sigma_e > \sigma_{ec} \end{cases} \quad (\text{E2})$$

which gives a relation that resembles the one described by Bandis *et al.* [54], but it is exactly linear at low values of effective stress. Problems that involve fractures that close or open might converge more readily using the linear relation (E2) than the Bandis model (E1). However, (E2) could give peculiar results if σ_e increases and exceeds σ_{ec} during the simulation because the effective normal stiffness can increase sharply over this transition in σ_e (as in the fracture propagation example described in the main text).

APPENDIX F: CONTACT APERTURE

Contact aperture, δ_o , varies over a fracture face depending on the details of slight shear displacements, amplitude of asperities or roughness, or other factors that cause misalignment of opposing fracture walls. Contact aperture could also result from bridges between fracture segments. A simple approach is to assume the contact aperture increases with distance from the fracture tip according to

$$\delta_o(x_1) = \delta_* \left(1 - \left(\frac{x_1}{a} \right)^2 \right)^{1/2} \quad (\text{F1})$$

where δ_* is the contact aperture at the mouth of the fracture. This implies that the misalignment between fracture walls is scale dependent, increasing with the size of the fracture, which seems reasonable for many cases. Alternative forms of (F1) can readily be included.

Details of the effects of a fracture closing on proppant can be simulated using this code by using parameters in (E1) and (E2) that represent proppant deformation, and by using (F1), or a similar relation, to express the distribution of proppant in the fracture.

APPENDIX G: IMPLEMENTING THE PROPAGATION CRITERION

Finding P_{tip}

A general iterative approach to find P_{tip} such that $K_I \approx K_{Ic}$ is based on the method of mid-sections:

Step 1: Calculate K_{I1} using the $P_1 = P_{\text{tip}}$ from the previous time step.

Step 2: Calculate K_{I2} using $P_2 = P_{\text{tip}}/2$.

Step 3: Calculate K_{Im} using $P_m = (P_1 + P_2)/2$.

Step 4: If $K_{I2} < K_{IC} < K_{Im}$, then set $K_{I1} = K_{Im}$ and recalculate K_{Im} using $P_m = (P_m + P_2)/2$ else
If $K_{Im} < K_{IC} < K_{I1}$, then set $K_{I2} = K_{Im}$ and recalculate K_{Im} using $P_m = (P_m + P_1)/2$.

Step 5: Repeat Step 4 until K_I is within a tolerance value of K_{IC} (e.g. ± 0.001).

This approach is robust, but it can require as many as ~ 10 calculations of K_I to converge using a tolerance of ± 0.001 . An alternative method that can converge faster than 10 steps uses linear interpolation as follows:

Step 1: Calculate K_{I1} using the $P_1 = P_{tip}$ from the previous time step.

Step 2: Calculate K_{I2} using $P_2 = CP_{tip}$, where $C < 1$ is a chosen positive number.

Step 3: Calculate $P_m = P_{tip} + (P_2 - P_1)(K_{IC} - K_{I2}) / (K_{I2} - K_{I1})$.

Step 4: Calculate K_{Im} using P_m and compare to tolerance.

Step 5: If necessary, let $P_1 = P_2$, $P_2 = P_m$, and repeat steps 3 and 4.

This method typically converged after Step 3 for $C = 0.95$, suggesting that K_I is nearly a linear function of P_{tip} for the problems we have evaluated.

Propagation

The logic used to implement propagation is as follows:

Step 1: Iteratively find P_{tip} such that $K_I = K_{IC}$ within a tolerance. Use the procedure above.

Step 2: Revise Δt during each iteration for P_{tip} using (2).

Step 3: Check that Δt has changed between successive iterations by less than a tolerance (e.g. ± 0.01).

Step 4: Use the iterative procedure in Step 1 to calculate two more values of P_{tip} , K_I , and Δt .

Step 5: Check that K_I and Δt criteria as in Steps 1 and 3 are satisfied. Return to Step 4 as needed.

The procedure outlined above required four to seven calculations of K_I for most problems.

APPENDIX H: DISCRETIZATION

The fracture and enveloping matrix are discretized using a rectangular grid with a variable spacing of M columns and N rows. The initial fracture lies along the lower row of the grid and is discretized into short segments. The matrix is discretized into blocks, and the widths of individual columns of blocks are the same as the length of the segment in the adjacent fracture. The grid is node-centred, so all the calculations are taken at the centre of the blocks in the matrix or segments along the fracture. The grids are either cartesian or axisymmetric, depending on the geometry of the fracture, with x_1 along the rows and x_2 along the columns.

The problems are assumed to be symmetric both about a plane through the fracture and about the borehole. Only one quarter of the matrix is represented in the grid as a result of symmetry. The full aperture of the fracture is represented by each segment, but only enough segments are used to represent half of the fracture.

The fracture is assumed to propagate in its initial plane, so the fracture will always stay within the same row. A segment and column of matrix blocks is added each time the fracture propagates. As a result, the size of the grid increases during propagation and this will increase

the computation time of each time step. A moving grid was considered to reduce computation time associated with the expanding grid during propagation. Leakoff into partially saturated conditions is difficult to represent in a moving grid because the relationship between saturation and pressure is non-linear, so using a moving grid was infeasible.

The fracture occurs in the bottom row of the grid (Figure 2), with the mouth of the fracture in the first column and the tip in the last one. Problems where fractures propagated were typically set up using segments of uniform width along the initial fracture, and geometrically increasing width along the propagating fracture. The height of rows is small adjacent to the fracture and they increase geometrically with distance from the fracture (Figure 2).

The width of the segment (or column) at the fracture tip increases as the fracture grows in order to improve efficiency of the solution during propagation. We recognize that this progressively diminishes resolution of fluid flow in the tip region of a hydraulic fracture during propagation. This is an inevitable consequence of using a fixed grid to represent partially saturated conditions in the matrix.

APPENDIX I: NOMENCLATURE

a	half-length of fracture
a_i	initial half-length of fracture
b, c	boundaries of interval on fracture bearing driving pressure $P_{d,bc}$
C_f	friction coefficient during fluid flow in fracture
E	Young's modulus
$E(u,t)$	elliptic integral of the second kind
E'	$E/(1-\nu^2)$
$F(u,t)$	elliptic integral of the first kind
h	hydraulic head in matrix
h_f	hydraulic head in fracture
h_o	initial hydraulic head
h_w	hydraulic head in well
H_f	height of a rectangular fracture
K	hydraulic conductivity
K_I	stress intensity factor
K_{sat}	saturated hydraulic conductivity
K_{Ic}	fracture toughness
K_{ni}	normal stiffness of fracture at initial contact of asperities
K_s	saturated hydraulic conductivity of matrix
L	entry length at mouth of fracture
m	number of the time step in Table I, number of grid points along fracture in Appendix C
M	number of segments of fracture or columns in grid
M_T	total mass of fluid injected into fracture
n	term affecting shape of capillary pressure and relative permeability relations
N	number of rows in grid
P	fluid pressure measured relative to P_a
P_a	atmospheric pressure

P_d	driving pressure on fracture face
P_{d1}	driving pressure over interval $b < x_1 < c$ in (C1)
P_e	air-entry pressure for the matrix
P_{initial}	initial pore pressure in the matrix
P_o	reference pressure for fluid density
P_s	steady pressure at mouth of fracture in A8
P_{tip}	pressure at the fracture tip
P_w	pressure in the wellbore at the elevation of the fracture
q_{well}	fluid flux into fracture at the well
q	volumetric flux or average velocity within the fracture
q_L	leakoff flux out of the fracture
q_n	volumetric flux in the n direction in matrix
Q	volumetric flow rate
Q_{pi}	volumetric flowrate of fluid into well
r_c	radius of the casing
r_w	radius of wellbore where the fracture mouth intersects the well
S	storativity
S_s	specific storage of matrix, from compressibility of solid and fluid
$S(h)$	$\partial\theta/\partial h$
t	time
T	fracture transmissivity
Δt	time step
V_g	volume of gas trapped in pumping system or wellbore
V_s	volume of fluid stored in pumping system
x_n	spatial coordinate; $x_1 = x$ for plane-strain case, $x_1 = r$ for axisymmetric case. Coordinate normal to fracture is x_2 for both cases
$x_{1,\text{max}}, x_{2,\text{max}}$	maximum values of coordinate
z	vertical distance used to calculate hydraulic head
<i>Greek letters</i>	
α	ratio of open area/total area of fracture
α_v	term affecting shape of capillary pressure and relative permeability relations
β	fluid compressibility
γ	unit weight of fluid
δ_c	mechanical aperture from local deformation of asperities
δ_g	mechanical aperture from global deformation of fracture walls
δ_{min}	minimum fracture aperture at high effective stress
δ_o	mechanical fracture aperture at initial contact of asperities
δ_p	global aperture due to driving pressure applied over a small increment
δ	fracture aperture
δ^*	contact aperture at mouth of fracture
δ_{slot}	aperture of initial slot
θ_{sat}	saturated water content of matrix
Δ	small extension of the fracture length in (A10)
ε	zero tolerance for effective stress in numerical scheme used in Table I
θ	volumetric water content in matrix

θ_r	residual volumetric water content in matrix
θ_s	saturated volumetric water content in matrix, at $P = 0$
Θ	penalty constant in numerical scheme used in Table I
μ	dynamic viscosity
ν	Poisson's ratio
ρ	x_1/a
ρ_f	density of fluid in the fracture
ρ_o	fluid density at a reference pressure
σ_c	confining stress
σ_e	effective stress on wall of fracture
σ_{ec}	aperture is a linear function of σ_e , where $\sigma_e < \sigma_{ec}$

ACKNOWLEDGEMENTS

We appreciate support CMC-0421090, from the National Science Foundation under grants EAR 9876124 and EAR 0001146 to LCM, and OCE-0221974, and OCE-0242163 to LNG.

REFERENCES

1. NRC. *Rock Fractures and Fluid Flow*. National Academy Press: Washington, 1996.
2. Gidley JL, Holditch SA, Nierode DE, Veatch RW. Recent advances in hydraulic fracturing. *Society Petroleum Engineers Monograph*, 452. Society of Petroleum Engineers, Dallas, 1989.
3. Economides MJ, Notte KG. *Reservoir Stimulation* (3rd Edition) Wiley: Chichester, U.K., 2000.
4. Murdoch LC, Wilson D, Savage K, Slack W, Uber J. Alternative methods for fluid delivery and recovery. *USEPA/625/R-94/003*. U.S. Environmental Protection Agency, 1994.
5. Murdoch LC, Slack WW. Forms of hydraulic fractures in shallow, fine-grained formations. *Journal of Geoenvironmental and Geotechnical Engineering* 2002; **128**:479–487.
6. Amadei B, Stephansson O. *Rock Stress and its Measurement*. Chapman & Hall: New York, 1997.
7. Rummel J, Hansen J. Interpretation of hydrofrac pressure recordings using a simple fracture mechanics simulation model. *International Journal of Rock Mechanics and Mining Sciences and Geomechanics Abstracts* 1989; **26**:483–488.
8. Haimson B, Fairhurst C (eds). *In-situ Stress Determination at Great Depth by Means of Hydraulic Fracturing*. The American Institute of Mining, Metallurgical, and Petroleum Engineers: New York, 1970.
9. Long JCS, Remer CR, Wilson CR, Witherspoon PA. Porous media equivalents for networks of discontinuous fractures. *Water Resources Research* 1982; **18**:645–658.
10. Barenblatt GI, Entov VM, Ryzhik VM. *Theory of Fluid Flows through Natural Rocks*. Kluwer Academic Publishers: Dordrecht, Boston, London, 1990; 395.
11. Earlougher RC. *Advances in Well Test Analysis*. Society of Petroleum Engineers, Dallas, 1977.
12. Kruseman GP, deRitter NA. Analysis and evaluation of pumping test data. *International Institute Land Reclamation Improvement*, Wageningen, Netherlands, 1991.
13. Warren JE, Root PJ. The behavior of naturally fractured reservoirs. *Society of Petroleum Engineer Journal* 1963; **3**:245–255.
14. Boulton NS, Streltsova TD. Unsteady flow to a pumped well in a fissured water-bearing formation. *Journal of Hydrology* 1977; **35**:257–269.
15. Moench AF. Double porosity models for a fissured groundwater reservoir with fracture skin. *Water Resources Research* 1984; **20**:831–846.
16. Sageev A. Slug test analysis. *Water Resources Research* 1986; **22**:1323–1333.
17. Grader A, Ramey HJ. Slug test analysis in dual porosity reservoirs. *SPE Formation Evaluation* 1988; v.3 n.2 329–339.
18. Rutqvist J. Coupled stress-flow properties of rock joints from hydraulic field testing. *Ph.D. Dissertation*, Royal Institute of Technology, Stockholm, 1995.
19. Chiles J-P, de Marsily G. Stochastic models of fracture systems and their use in flow and transport modeling. In *Flow and Contaminant Transport in Fractured Rock*, Bear J, Tsang CF, de Marsily G (eds). Academic Press: New York, 1993; 169–236.

20. Barthelemy P, Jacquin C, Yao J, Thovert J-F, Adler PM. Hierarchical structures and hydraulic properties of a fracture network in the Cuasse of Larzac. *Journal of Hydrology* 1990; **187**:237–258.
21. Renshaw CE. Influence of sub-critical fracture growth on the connectivity of fracture networks. *Water Resources Research* 1996; **32**:1519–1530.
22. Adler PM, Thovert J-F. *Fractures and Fracture Networks*. Kluwer Academic Publishers: Dordrecht, 1999.
23. Smith L, Schwartz FW. Solute transport through fracture networks. In *Flow and Contaminant Transport in Fractured Rock*, Bear J, Tsang CF, de Marsily G (eds). Academic Press: New York, 1993; 129–165.
24. Cacas MC, Ledoux E, de Marsily G, Barbreau A, Calmels P, Gaillard B, Margritta R. Modeling fracture flow with a stochastic discrete fracture network; calibration and validation. *Water Resources Research* 1990; **26**(3):491–500.
25. Bogdanov II, Mourzenko VV, Thovert J-F, Adler PM. Pressure drawdown well tests in fractured porous media. *Water Resources Research* 2003; **39**:1021.
26. Koudina N, Gonzalez Garcia R, Thovert J-F, Adler PM. Permeability of three-dimensional fracture networks. *Physical Review E. Statistical Physics, Plasmas, Fluids, and Related Interdisciplinary Topics* 1998; **57**:4466–4479.
27. Germanovich LN, Astakhov DK. Stress-dependent permeability and fluid flow through parallel joints. *Journal of Geophysical Research—Solid Earth* 2004; **109**(B9):Art. No. B09203.
28. Germanovich LN, Astakhov DK. Fracture closure in extension and mechanical interaction of parallel joints. *Journal of Geophysical Research—Solid Earth* 2004; **109**(B2):Art. No. B02208.
29. Zhang J, Roegiers J-C, Spetzler HA. Influence of stress on permeability around a borehole in fractured porous media. *International Journal of Rock Mechanics and Mining Sciences* 2004; **41**:2–6.
30. Raghavan R, Chin LY. Productivity changes in reservoirs with stress-dependent permeability. *SPE Reservoir Evaluation and Engineering* 2004; **7**:308–315.
31. Bai M, Meng F, Elsworth D, Zaman Z, Roegiers J-C. Numerical modeling of stress-dependent permeability. *International Journal of Rock Mechanics and Mining Sciences* 1997; **34**:446.
32. Wilcock P. Generic study of coupled T-H-M processes in the near-field (BMT3). In *Coupled Thermo-Hydromechanical Processes of Fractured Media*, Stephansson O, Jing L, Tsang C-F (eds). Elsevier: Amsterdam, 1996; 213–230.
33. Herbert AW. Modeling approaches for discrete fracture network flow analysis. In *Coupled Thermo-Hydromechanical Processes of Fractured Media*, Stephansson O, Jing L, Tsang C-F (eds). Elsevier: Amsterdam, 1996; 213–230.
34. Unger AJA, Mase CW. Numerical study of the hydromechanical behavior of two rough fracture surfaces in contact. *Water Resources Research* 1993; **29**:2101–2114.
35. Mourzenko VV, Galamay O, Thovert J-F, Adler PM. Fracture deformation and influence on permeability. *Physical Review E. Statistical Physics, Plasmas, Fluids, and Related Interdisciplinary Topics* 1997; **56**:3167–3184.
36. Bogdanov II, Mourzenko VV, Thovert J-F, Adler PM. Effective permeability of fractured porous media in steady state flow. *Water Resources Research* 2003; **39**:1023.
37. Germanovich LN, Astakhov DK, Shlyapobersky J, Mayerhofer MJ, Dupont C, Ring LM. Modeling multi-segmented hydraulic fracture in two extreme cases: no leak-off and dominating leak-off. *International Journal of Rock Mechanics and Mining Sciences* 1998; **35**(4–5):551–554.
38. Valko P, Economides MJ. *Hydraulic Fracture Mechanics*. Wiley: New York, 1995.
39. Sousa JL, Carter BJ, Ingraffea AR. Numerical simulation of 3D hydraulic fracture using Newtonian and power-law fluids. *International Journal of Rock Mechanics and Mining Sciences and Geomechanics Abstracts* 1993; **30**:1265–1271.
40. Detournay E. Fluid and solid singularities at the tip of a fluid-driven fracture. In *Non-Linear Singularities in Deformation and Flow*, Durban D, Pearson J (eds). Kluwer Academic Publishers: Dordrecht, 1999; 27–42.
41. Carbonell R, Desroches J, Detournay E. A comparison between a semianalytical and a numerical solution of a two-dimensional hydraulic fracture. *International Journal of Solids and Structures* 1999; **36**(31–32):4869–4888.
42. Garagash D, Detournay E. Near tip processes of a fluid-driven fracture. *Journal of Applied Mechanics* 2000; **67**:183–192.
43. Garagash D, Detournay E. Tip region of a fluid-driven fracture in an elastic medium. *Journal of Applied Mechanics—Transactions of the ASME* 2000; **67**:183–192.
44. Savitski A, Detournay E. Propagation of a penny-shaped fluid-driven fracture in an impermeable rock: asymptotic solutions. *International Journal of Solids and Structures* 2002; **39**(26):6311–6337.
45. Adachi JJ. Fluid-driven fracture in permeable rock. *Ph.D. Thesis*, University of Minnesota, 2001.
46. Carter RD. Optimum fluid characteristics for fracture extension. Appendix to paper by Howard CC, Fast CR, *Drilling and Production Practice* 1957; **API**:267.
47. Neuzil CE, Tracy JV. Flow through fractures. *Water Resources Research* 1981; **17**:191–199.
48. Cook AM, Meyer LR, Cook NGW, Doyle FM. The effect of tortuosity on flow through a natural fracture. In *Rock Mechanics Contributions and Challenges*, Hustrulid WA, Johnson GA (eds), *Proceedings of the 31st U.S. Symposium on Rock Mechanics*. A.A. Balkema: Rotterdam, 1990.
49. Renshaw CE. On the relationship between mechanical and hydraulic apertures in rough-walled fractures. *Journal of Geophysical Research* 1995; **100**:24629–24636.

50. Zimmerman RW, Main I. Hydromechanical behavior of fractured rocks. In *Mechanics of Fluid-saturated Rocks*, Gueguen Y, Bouteica M (eds). Elsevier: Boston, 2004; 363–421.
51. Pyrak-Nolte LJ, Morris JP. Single fractures under normal stress; the relation between fracture specific stiffness and fluid flow. *International Journal of Rock Mechanics and Mining Sciences and Geomechanics Abstracts* 2000; **37**:245–262.
52. Rice JR. Mathematical analysis in the mechanics of fracture. In *Fracture, An Advanced Treatise*, Leibowitz H (ed.). Academic Press: New York, 1968; 172–308.
53. Germanovich LN, Dyskin AV. Virial expansions in problems of effective characteristics. Part I: general concepts. *Mechanics of Composite Materials* 1994; **30**(2):157–167.
54. Bandis SC, Lumsen AC, Barton NR. Fundamentals of rock joint deformation. *International Journal of Rock Mechanics and Mining Sciences and Geomechanics Abstracts* 1983; **20**:249–268.
55. Papanastasiou P. The influence of plasticity in hydraulic fracturing. *International Journal of Fracture* 1997; **84**:61–79.
56. Durban D, Papanastasiou P. Singular crack-tip fields for pressure sensitive plastic solids. *International Journal of Fracture* 2003; **119**:47–63.
57. Chang H. Hydraulic fracturing in particulate materials. *Ph.D. Thesis*, Georgia Institute of Technology, Atlanta, 2004.
58. Detournay E, Cheng AH-D, Roegiers J-C, McLennan JD. Poroelasticity considerations in *in situ* stress determination by hydraulic fracturing. *International Journal of Rock Mechanics and Mining Sciences and Geomechanics Abstracts* 1989; **26**:507–513.
59. Boone TJ, Ingraffea AR, Roegiers JC. Visualization of hydraulically driven fracture propagation in poroelastic media using a superworkstation. *Journal of Petroleum Technology—Transactions of AIME* 1989; **41**:574–580.
60. Detournay E, Cheng A. Plane strain analysis of a stationary hydraulic fracture in a poroelastic medium. *International Journal of Solids and Structures* 1991.
61. Germanovich LN, Roegiers J-C. Discussion of a continuum-damage-mechanics model of hydraulic fracturing. *Journal of Petroleum Technology* 1993; 1190–1191, V.15, N.12.
62. Geertsma J, de Klerck F. A rapid method of predicting the extent of hydraulically induced fractures. *Journal of Petroleum Technology* 1969; **21**:1571–1581.
63. Murdoch LC. Hydraulic fracturing of soil during laboratory experiments: methods and observations. *Geotechnique* 1993; **42**:255–265.
64. Murdoch LC. Hydraulic fracturing of soil during laboratory experiments: propagation. *Geotechnique* 1993; **43**:266–276.
65. Murdoch LC. Hydraulic fracturing of soil during laboratory experiments: theoretical analysis. *Geotechnique* 1993; **43**:277–287.
66. Harison JA, Hardin BO, Mahboub K. Fracture toughness of compacted cohesive soils using a ring test. *Journal of Geotechnical Engineering* 1994; **120**:872–891.
67. Murdoch LC. Mechanical analysis of an idealized hydraulic fracture at shallow depths. *Journal of Geoenvironmental and Geotechnical Engineering* 2002; **128**:488–495.
68. Nilson RH, Griffiths SK. Similarity analysis of energy transport in gas-driven fractures. *International Journal of Fracture* 1986; **30**:115–134.
69. Powell MJD. A hybrid method of nonlinear equations. In *Numerical Methods for Nonlinear Algebraic Equations*, Rabinowitz P (ed.). Gordon and Breach: London, 1970; 87–114.
70. Garbow B, Hillstom K, More J. MINPACK. in. www.netlib.org/minpack, Argonne National Lab, 1980.
71. Dent D, Paprzycki M, Kucaba-Pietal A. Studying the performance of nonlinear systems solvers applied to the random vibration test. *3rd International Conference on Large-Scale Scientific Computing*, 2002; 473–478.
72. Butler JJ. *The Design, Performance, and Analysis of Slug Tests*. Lewis Publishers: Boca Raton, 1998.
73. Murdoch LC, Schweisinger T, Svenson E, Germanovich L. Measuring and analyzing transient changes in fracture aperture during hydraulic well tests: preliminary results. *Second International Symposium on Dynamics of Fluids in Fractured Rock*, Berkeley, CA, 2004; 129–132.
74. Murdoch LC, Svenson E, Schweisinger T. Slug tests in deformable fractures. *12th Annual Clemson Hydrogeology Symposium*, Clemson, SC, 2004.
75. Cooper HH, Bredehoeft JD, Papadapolous IS. Response of a finite diameter well to an instantaneous charge of water. *Water Resources Research* 1967; **3**:263–269.
76. van Dam DB, Papanastasiou P, de Pater CJ. Impact of rock plasticity on hydraulic fracture propagation and closure. *SPE Production and Facilities* 2002; **17**:149–159.
77. Papanastasiou P. Hydraulic fracture closure in pressure-sensitive elastoplastic medium. *Journal of Fracture* 2000; **103**:149–161.
78. Gulrajani SN, Nolte KG. Fracture evaluation using pressure diagnostics. In *Reservoir Stimulation*, Economides MJ, Nolte KG (eds). Wiley: New York, 2000; 9–1–A9–16.
79. Bjerrum L, Andersen KH. *In-situ* measurement of lateral pressures in clay. *Geotechnique* 1972; **15**:11–20.

80. Massarch KR. New aspects of soil fracturing in clay. *Journal of the Geotechnical Engineering Division* 1978; **GT8**:1109–1123.
81. Malin SC. In situ stress determination in unsaturated soils using hydraulic fractures. *M.S. Thesis*, Clemson University, Clemson, 2005, 150 p.
82. Mack MG, Warpinski NR. Mechanics of hydraulic fracturing. In *Reservoir Stimulation*, Economides MJ, Nolte KG (eds). Wiley: New York, 2000; 6-1–6-49.
83. Gilmore P, Kelley CT. An implicit filtering algorithm for optimization of functions with many local minima. *SIAM Journal on Optimization* 1995; **4**:269–285.
84. Press WH, Flannery BP, Teukolsky SA, Vetterling WT. *Numerical Recipes*. Cambridge University Press: Cambridge, 1989.
85. Germanovich LN, Van Dyke PE, Chang H, Wu R. Hydraulic fractures in particulate materials. *International Journal of Rock Mechanics and Mining Sciences* 2006; in preparation.
86. Economides MJ, Nolte KG. *Reservoir Stimulation* (3rd edn). Wiley: Chichester, U.K., 2000.
87. Witherspoon PA, Wang JSY, Iwai K, Gale JE. Validity of cubic law for fluid flow in a deformable rock fracture. *Water Resources Research* 1980; **16**:1016–1024.
88. Zimmerman RW, Chen D, Cook NGW. The effect of contact area on the permeability of fractures. *Journal of Hydrology* 1992; **139**:79–96.
89. Walsh JB. Effect of pore pressure and confining pressure on fracture permeability. *International Journal of Rock Mechanics and Mining Sciences and Geomechanics Abstracts* 1981; **18**:429–435.
90. Wu R, Germanovich LN, Van Dyke PE, Lowell RP. A laboratory technique for controlling hydraulic fractures. *Journal of Geophysical Research* 2006, (in press).
91. Desroches J, Carter BJ. Three-dimensional modeling of a hydraulic fracture. *North American Rock Mechanics Symposium, NARMS'96*, Montreal, 1996; 995–1002.
92. Desroches J, Lenoach B, Papanastasiou P, Theirclin M. On the modeling of near tip processes in hydraulic fractures. *International Journal of Rock Mechanics and Mining Sciences and Geomechanics Abstracts* 1993; **30**(7):1127–1134.
93. Detournay E, Garagash DI. The near tip region of a fluid-driven fracture propagating in a permeable elastic solid. *Journal of Fluid Mechanics* 2003; **494**:1–32.
94. van Genuchten MT. A closed-form equation for predicting the hydraulic conductivity of unsaturated soil. *Soil Science Society of America Journal* 1980; **44**:892–898.
95. Tada H, Paris PC, Irwin GR. *The Stress Analysis of Cracks Handbook* (2nd edn). Paris Productions Inc.: St. Louis, MO, 1985.
96. Sneddon IN. *Fourier Transforms*. Dover Publications: New York, 1995; 541.
97. Gradshteyn IS, Ryzhik IM. *Table of Integrals, Series and Products*. Academic Press: New York, 1965.
98. Greenwood JA, Tripp JH. The contact of two nominally flat rough surfaces. *Proceedings of the Institution of Mechanical Engineers* 1970; **185**:625–633.